

Article

# Extremely Robust Remote-Target Detection Based on Carbon Dioxide-Double Spikes in Midwave Spectral Imaging

Sungho Kim <sup>1,\*</sup> , Jungsub Shin <sup>2</sup>, Joonmo Ahn <sup>2</sup> and Sunho Kim <sup>2</sup>

<sup>1</sup> Department of Electronic Engineering, Yeungnam University, 280 Daehak-Ro, Gyeongsan, Gyeongbuk 38541, Korea

<sup>2</sup> Agency for Defense Development, P.O. Box 35, Daejeon 34186, Korea; jss@add.re.kr (J.S.); ahnjm@add.re.kr (J.A.); edl423@add.re.kr (S.K.)

\* Correspondence: sunghokim@ynu.ac.kr; Tel.: +82-53-810-3530

Received: 6 April 2020; Accepted: 15 May 2020; Published: 20 May 2020



**Abstract:** Infrared ship-target detection for sea surveillance from the coast is very challenging because of strong background clutter, such as cloud and sea glint. Conventional approaches utilize either spatial or temporal information to reduce false positives. This paper proposes a completely different approach, called carbon dioxide-double spike (CO<sub>2</sub>-DS) detection in midwave spectral imaging. The proposed CO<sub>2</sub>-DS is based on the spectral feature where a hot CO<sub>2</sub> emission band is broader than that which is absorbed by normal atmospheric CO<sub>2</sub>, which generates CO<sub>2</sub>-double spikes. A directional-mean subtraction filter (D-MSF) detects each CO<sub>2</sub> spike, and final targets are detected by joint analysis of both types of detection. The most important property of CO<sub>2</sub>-DS detection is that it generates an extremely low number of false positive caused by background clutter. Only the hot CO<sub>2</sub> spike of a ship plume can penetrate atmosphere, and furthermore, there are only ship CO<sub>2</sub> plume signatures in the double spikes of different spectral bands. Experimental results using midwave Fourier transform infrared (FTIR) in a remote sea environment validate the extreme robustness of the proposed ship-target detection.

**Keywords:** ship detection; false alarm; carbon dioxide peaks; midwave infrared; FTIR

## 1. Introduction

Remote-ship detection is important in various applications, such as maritime navigation [1], coast guard searches [2], and homeland security procedures [3]. Infrared images are frequently adopted, especially due to their operational capability, day or night.

The key issue is how to reduce the high number of false detections caused by cloud clutter and sea surface glint while maintaining an acceptable detection rate [4,5]. Cloud edges produce false detections, and sea glint is similar to small infrared targets, both of which degrade detection performance. Since the 1990s, a lot of methods have been proposed to reduce the false positives by using either spatial information or temporal information from infrared images.

Spatial information processing, such as background subtraction, can be a feasible approach to reducing background clutter. Background images are estimated by spatial filters, such as the mean filter [6], the least mean square filter [7,8], the median filter [9], and the morphological filter [10]. These filters use neighboring pixels to estimate background pixel values, but with different strategies. In particular, mean subtraction filter (MSF)-based target detection is the most simple, but is weak when it comes to cloud edges. Non-linear filters, such as max-median, morphology, and data-fitting, show better cloud clutter suppression capabilities [11,12]. Local directional

Laplacian-of-Gaussian filtering can remove false positives from cloud edges [13]. In the spatial information approach, classification with a spatial shape feature can discriminate clutter. Hysteresis thresholding [14], statistics-based adaptive thresholding [15], the Bayesian classifier [16], and support vector machines [17] are well-known methods. Voting by various classifiers can enhance dim-target detection rates [18]. Spatial frequency information can be used to remove low-frequency clutter, such as the three-dimensional fast Fourier transform (3D-FFT) spectrum [19]. The wavelet transform is effective against sea glint [20], and low pass filter can also deal with sea glint [21]. An adaptive high-pass filter can reduce cloud and sea glint clutter [22], while spatial target-background contextual information enhances the target signature and reduces background clutter, which is effective for sea glint reduction [23]. Spatial multi-feature fusion can increase the clutter discrimination capability [24].

Temporal information processing, such as track-before-detection, can remove slowly moving cloud clutter and fast-blinking sea glint [25]. Temporal profiles are useful to discriminate between a fast-moving target and slow-moving cloud [26–28]. The temporal contrast filter is suitable for detecting small, supersonic, infrared targets [29], and a 3D matched filter for wide-to-exact searches can remove cloud clutter very fast [30]. A power-law detector for image frames is effective for target detection in dense clutter [31]. Since a previous frame can be regarded as background, a weighted autocorrelation matrix update using the recursive technique can be useful in order to eliminate sea glint [32]. An advanced adaptive spatial-temporal filter can achieve tremendous gain [33], and principal component analysis in multi-frames can alleviate false positives from sun glint [34].

Synthetic aperture radar (SAR) with deep learning can be a useful approach for remote ship detection application [35–37]. Faster R-CNN [35], DRBox [36], and Contextual CNN [37] can provide improved detection performance but these approaches require huge number of training dataset to reduce false positives.

As mentioned above, the conventional approaches in the spatial- or temporal-image domains have their own pros and cons, depending on the situations and conditions. The spatial filter based approach relies on target shapes and intensity distributions, which is ambiguous if targets are far away. The temporal filter based approach assumes fast target motion with stationary sensors. If this assumption is not satisfied, it will generate many false positives in the maritime environment.

This paper proposes a novel spectral–spatial signature analysis-based ship detection method in midwave hyperspectral images, instead of the conventional spatial or temporal methods. Based on the combustion process, CO<sub>2</sub> emissions show a double-spike signature at around 4.16 μm (2400 cm<sup>-1</sup>) and 4.34 μm (2300 cm<sup>-1</sup>). The hot CO<sub>2</sub> emission band is broader than that which is absorbed by normal atmospheric CO<sub>2</sub>, which generates CO<sub>2</sub>-double spikes. The directional-mean subtraction filter (D-MSF) detects each CO<sub>2</sub> spike, and final targets are detected by joint analysis of the detection of both spikes. So, we call the proposed method carbon dioxide-double spike (CO<sub>2</sub>-DS) detection.

The contributions from this paper can be summarized as follows. First, the phenomenon of the CO<sub>2</sub>-double spike emission in the midwave band is analyzed systematically. Second, a novel spectral–spatial analysis is proposed to detect remote ships in the maritime environment based on this analysis. Third, CO<sub>2</sub>-DS detection can suppress background clutter (cloud, sea glints) completely, which leads to an extremely low false positive rate in remote-ship detection. Finally, the performance of CO<sub>2</sub>-DS detection is demonstrated in a real sea environment with real ships.

The remainder of this paper is organized as follows. Section 2 explains the proposed CO<sub>2</sub>-DS method, including analysis of carbon dioxide-double spike radiation. Section 3 evaluates the clutter suppression performance of the CO<sub>2</sub>-DS method in the maritime environment. The paper concludes in Section 4.

## 2. Proposed Ship CO<sub>2</sub> Plume Detection

### 2.1. Signature Analysis of Carbon Dioxide-Double Spikes

Before explaining the details of the proposed CO<sub>2</sub>-DS, the double-spike phenomenon in midwave spectral bands should be introduced [38,39]. Figure 1 summarizes the overall mechanism of CO<sub>2</sub>-double spikes in received spectral radiance from ship plumes. Hot CO<sub>2</sub> emits thermal energy in wider spectral band than that of normal air CO<sub>2</sub>, as shown in Figure 1a. Atmospheric spectral transmittance shows strong absorption at 2300–2380 cm<sup>-1</sup> by normal CO<sub>2</sub> in the atmosphere, as shown in Figure 1b. Therefore, the received spectral radiance in a TELOPS Fourier transform infrared (FTIR) camera [40] shows a double-spike signature: the first spike is around 2276 cm<sup>-1</sup> (4.39 μm), and the second spike is around 2393 cm<sup>-1</sup> (4.18 μm).

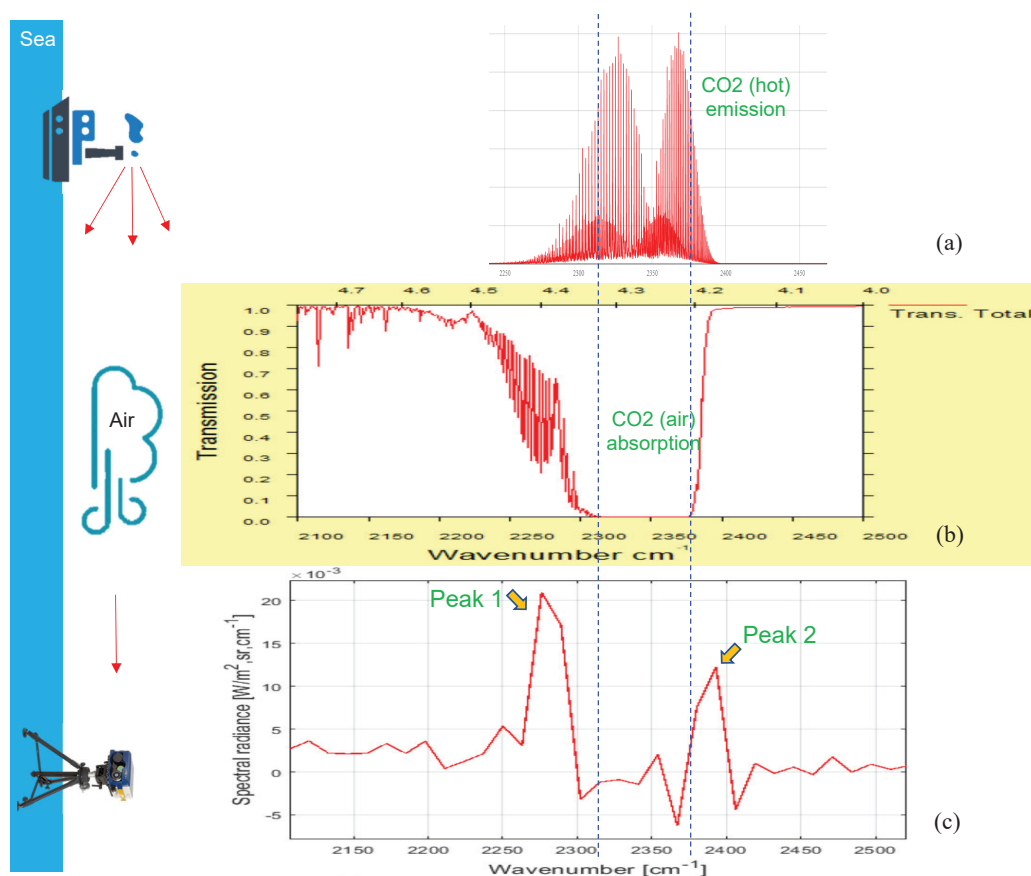


**Figure 1.** Operational concept of remote ship detection and the double spike-signature generation mechanism of hot carbon dioxide: (a) spectrum of a hot CO<sub>2</sub> emission by a ship, (b) spectral atmospheric transmittance, and (c) received spectral radiance of hot CO<sub>2</sub> from a ship's plume.

The measurement of CO<sub>2</sub>-double spikes can be derived from radiative transfer calculated with Equation (1). We adopted the radiative-transfer equation used in the Moderate-Resolution Atmospheric Radiance and Transmittance (MODTRAN) [41]. In general, at-sensor received radiance in the midwave infrared (MWIR) region consists of CO<sub>2</sub>-emitted radiance, transmitted background radiance, and total atmospheric path radiance (thermal+solar components).

$$L_{target}(\lambda) = \tau(\lambda) \left[ \varepsilon(\lambda) B_{CO_2}(\lambda, T_{CO_2}) + (1 - \varepsilon(\lambda)) L_{bg}(\lambda) \right] + L_s^\uparrow(\lambda) + L_{atm}^\uparrow(\lambda) \quad (1)$$

$L_{target}(\lambda)$  is the observed at-sensor target radiance;  $\lambda$  is wavelength;  $\varepsilon(\lambda)$  is spectral CO<sub>2</sub> gas emissivity;  $B_{CO_2}(\lambda, T_{CO_2})$  is the spectral radiance of the hot CO<sub>2</sub> gas, assuming a blackbody in the Planck function with the combusted CO<sub>2</sub> gas temperature ( $T_{CO_2}$ );  $\tau(\lambda)$  is the spectral atmospheric transmittance, and  $L_s^\uparrow(\lambda)$  and  $L_{atm}^\uparrow(\lambda)$  are the spectral upwelling solar and thermal path radiance, respectively, reaching the sensor.

According to the spectral emissivity of combusted CO<sub>2</sub> gas [38],  $\varepsilon(\lambda)$  is relatively high. Therefore, the term  $L_{bg}$  can be removed. According to MWIR radiometric characteristics [42], the contribution of solar radiance,  $L_s^\uparrow(\lambda_{CO_2})$ , from air scattering is very small, even for very dry conditions (less than 2% at 5  $\mu\text{m}$ ) [42]. Ignoring the solar term, we can simplify Equation (1) to Equation(2):

$$L_{target}(\lambda) = \tau(\lambda) [\varepsilon(\lambda)B_{CO_2}(\lambda, T_{CO_2})] + (1 - \tau(\lambda))B_{atm}(\lambda, T_{atm}) \quad (2)$$

where the definition of thermal upwelling,  $L_{atm}^\uparrow(\lambda)$ , is replaced by the multiplication of blackbody radiation of the atmosphere,  $B_{atm}(\lambda, T_{atm})$  and  $1 - \tau(\lambda)$ . The observed target spectral radiance,  $L_{target}$ , directly depends on both emissivity  $\varepsilon(\lambda)$  of hot CO<sub>2</sub>, and atmospheric transmittance,  $\tau(\lambda)$ , that should be analyzed specifically.

In addition, neighboring pixels to target hot CO<sub>2</sub> has only atmospheric spectral path radiance at wavelength  $\lambda$ . Therefore, the received background signal can be expressed with Equation (3):

$$L_{neighbor}(\lambda) = (1 - \tau(\lambda))B_{atm}(\lambda, T_{atm}) \quad (3)$$

If we apply center-surround difference by subtracting Equation (3) from Equation (2), which is the same as a mean subtraction filter (MSF) operation for a specific band image, the target-only signal can be extracted with Equation (4). This physical property is used in the D-MSF to extract the target (hot CO<sub>2</sub>) signature:

$$L_{targetOnly}(\lambda) = L_{target}(\lambda) - L_{neighbor}(\lambda) = \tau(\lambda) [\varepsilon(\lambda)B_{CO_2}(\lambda, T_{CO_2})] \quad (4)$$

Conventional ships are powered by diesel engines, and the corresponding hydrocarbon combustion produces water vapor, H<sub>2</sub>O) and CO<sub>2</sub> as expressed in Equation (5) [39,43]:



The first important parameter is spectral emissivity  $\varepsilon(\lambda)$  in Equation (2). The normal temperature of combusted CO<sub>2</sub> gas from ships is approximately 600 K by infrared signature suppression (IRSS) [44]. The emission band-width of CO<sub>2</sub> gas is proportional to the temperature of the CO<sub>2</sub> gas [39]. Figure 2 demonstrates this phenomenon by changing CO<sub>2</sub> temperature using the high-resolution transmission molecular absorption database (HITRAN) simulation on the web (<http://hitran.iao.ru/molecule/>). As the CO<sub>2</sub> temperature increases, the absorption band range is broader. The absorption band range of normal atmospheric temperature (300 K) is 2300–2380  $\text{cm}^{-1}$  (or 4.20–4.35  $\mu\text{m}$ ), where the inverse acts as atmospheric transmittance. The spectral unit can be either the wavelength ( $\lambda$ ) [ $\mu\text{m}$ ] or wavenumber ( $k$ ) [ $\text{cm}^{-1}$ ] by unit selection ( $k = 10,000/\lambda$ ). For hot CO<sub>2</sub>, the spectral absorption coefficient is the same as the spectral emission coefficient,  $\varepsilon(\lambda)$ , in Equation (2).

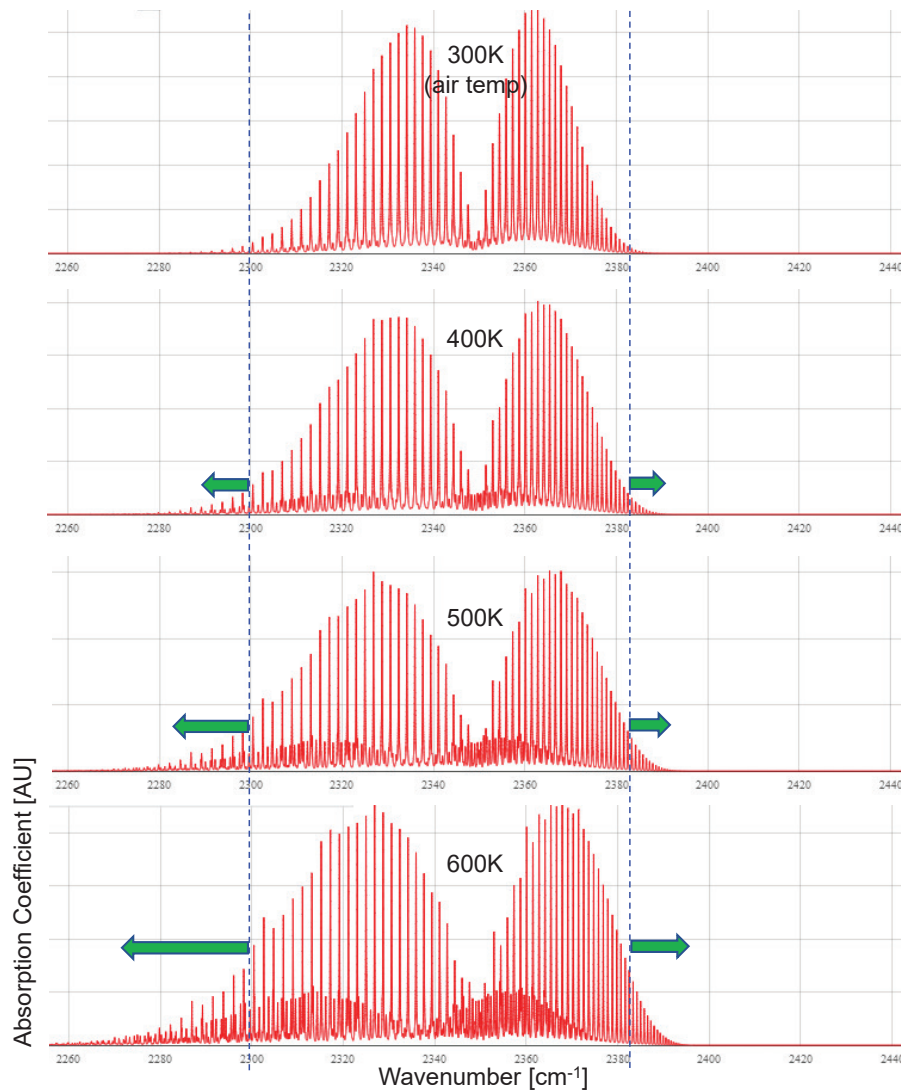


**Figure 2.** Spectral absorption coefficient variations of carbon dioxide according to different gas temperatures.

The second important parameter is spectral atmospheric transmittance  $\tau(\lambda)$  in Equation (2). In the MODTRAN simulation in the MWIR band, the spectral transmittance of the  $\text{CO}_2$  band ( $2320\text{--}2375\text{ cm}^{-1}$  or  $4.21\text{--}4.31\text{ }\mu\text{m}$ ) decreases abruptly with distance, as shown in Figure 3. The average transmittance in the  $\text{CO}_2$  band is 0.13, 0.005, and 0 at 5, 20, and 100 m, respectively. Note that the atmospheric transmittance band of zero value coincides with the spectral absorption coefficient of  $\text{CO}_2$  at 300 K in the top part of Figure 2. In addition, it remains only the atmospheric path radiance in Equation (2) in the  $\text{CO}_2$  absorption band,  $\tau(\lambda) = 0$ , where there is no target or background signals.

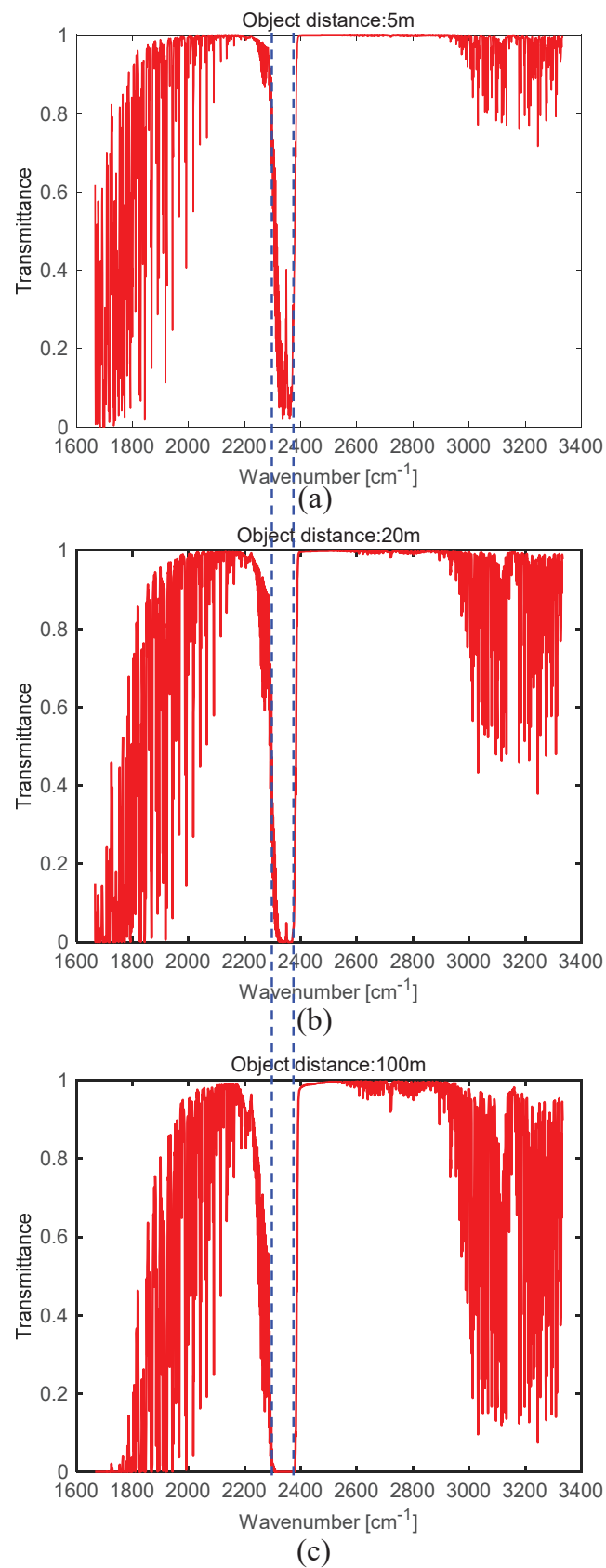


**Figure 3.** Spectral transmittance according to ship-camera distance in the MWIR band: (a) 5, (b) 20, and (c) 100 m.

Multiplication of the spectral emissivity of hot CO<sub>2</sub> and atmospheric transmittance produces double spikes, as shown in the bottom portion of Figure 1. The spectral feature where a hot CO<sub>2</sub> emission band is broader than that which is absorbed by normal atmospheric CO<sub>2</sub> generates CO<sub>2</sub> double spikes. The midwave spectral information is acquired via TELOPS MWIR hyperspectral camera [40]. It can provide calibrated spectral radiance images with a high spatial and spectral resolution from a Michelson interferometer in the short-wave to midwave bands (1.5–5.6 μm).

## 2.2. CO<sub>2</sub>-DS-Based Ship Plume Detection

Motivated by the double-spike phenomenon of hot CO<sub>2</sub>, a novel ship-detection method is proposed, as shown in Figure 4. The proposed method is called CO<sub>2</sub>-DS because it is based on the carbon dioxide-double spike feature. The proposed CO<sub>2</sub>-DS approach consists of three steps: spectral band selection, spatial small-target detection, and the final ship detection. The spectral band selection sets the search range in the spectral domain focusing on the CO<sub>2</sub> absorption band. Then, each CO<sub>2</sub> spike is detected by a carefully designed spatial filter (the directional-mean subtraction filter). Finally, the target ship is confirmed using a joint detection operation.

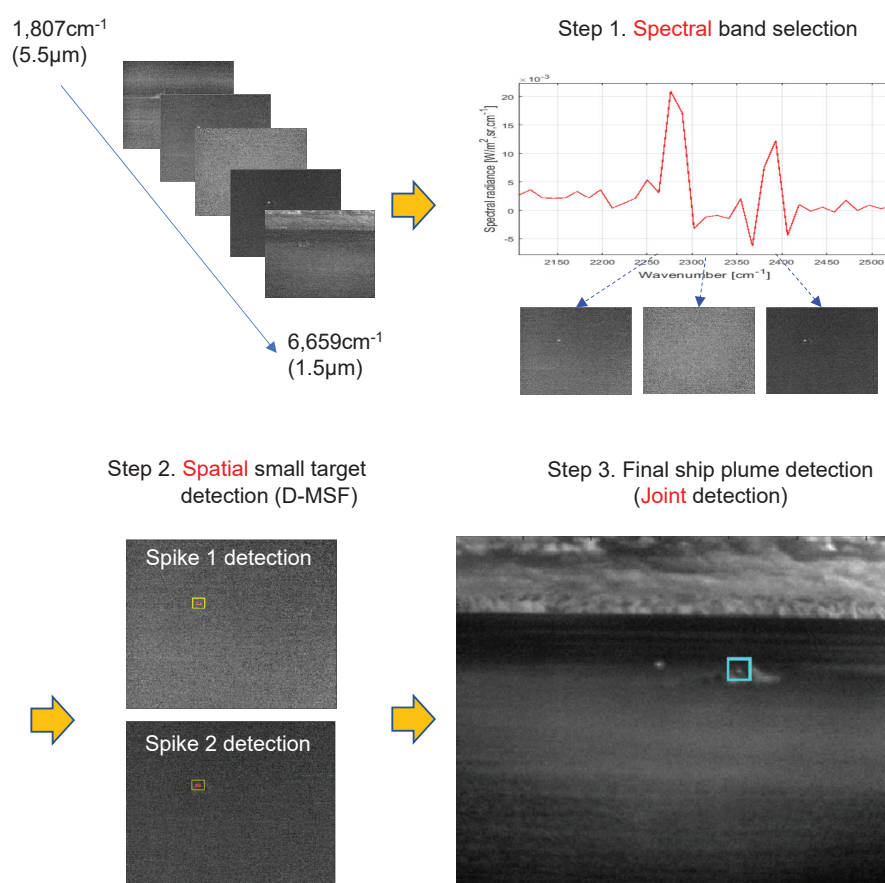


**Figure 4.** Overall processing flow of remote-ship detection using spectral-spatial information of hot CO<sub>2</sub> plumes.

In Step 1, the specific spectral band range should be defined to attain successful remote-ship detection with extremely few false positives. The proposed CO<sub>2</sub>-DS method is based on the atmospheric CO<sub>2</sub> absorption band (2320–2375 cm<sup>-1</sup> or 4.21–4.31 μm) that should be included. In addition, double-spike bands emitted by hot CO<sub>2</sub> should be included. The first spike range is below 2300 cm<sup>-1</sup>, and the second spike range is above 2380 cm<sup>-1</sup>.

The details of Step 2 and Step 3 in Figure 4 are described in Figure 5. Each spike signal is detected by a parallel search algorithm: the first spike detection and the second spike detection.

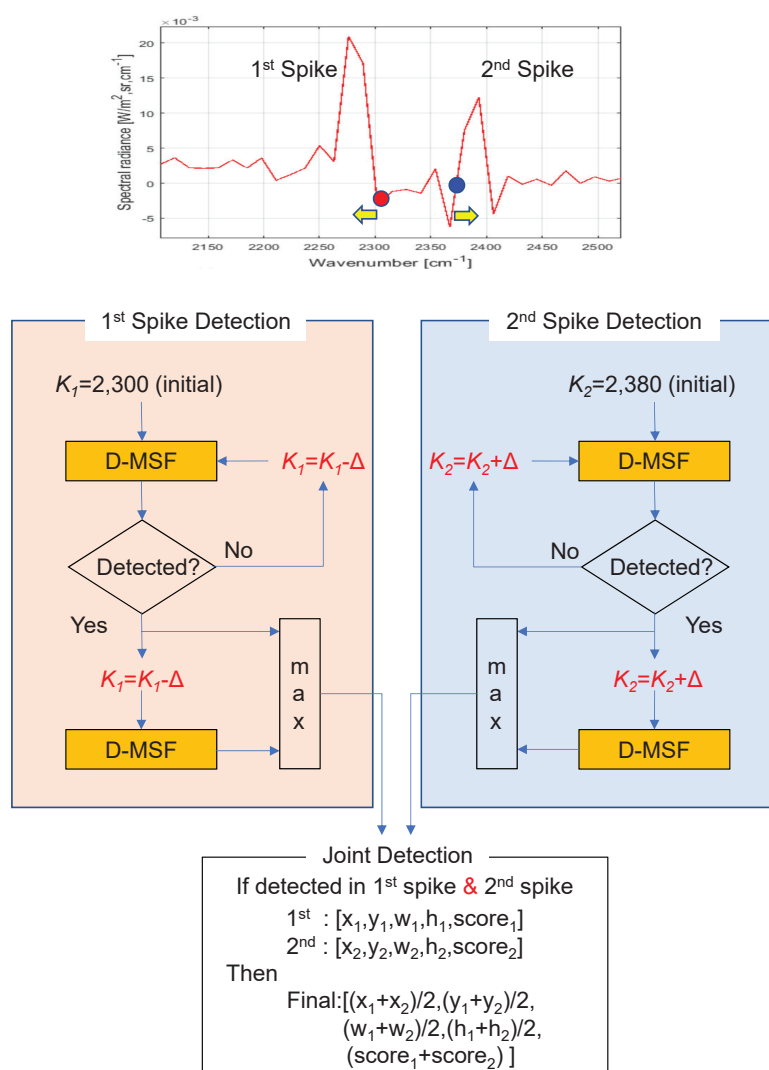


**Figure 5.** Details of the proposed CO<sub>2</sub>-DS: first spike detection, second spike detection, and joint detection.

The starting wavenumbers are 2300  $cm^{-1}$  and 2380  $cm^{-1}$  because there is no signal at all except for atmospheric path radiance. Given a wavenumber, a test image of this band is probed by D-MSF-based small infrared target detection [4]. D-MSF is adopted in this paper because it is a well-proven method and robust against thermal noise in the maritime environment. Figure 6 summarizes the detailed flow of the D-MSF graphically. Given a hypothesized spectral band image,  $I_\lambda(x, y)$ , a mean subtraction filter,  $h(x, y)$ , is used to enhance the signal-to-clutter ratio (1). Then, directional local median  $I_\lambda^D(x, y)$  is used to estimate row directional background (2) from the MSF result,  $I_\lambda^{MSF}(x, y)$ . Subtracting (2) from (1) in Figure 6 produces a clearer signature image. The region of interest (ROI) is generated by an initial thresholding ( $th1$ ) and eight-nearest neighbor-based clustering. Final detection is achieved by applying adaptive thresholding  $th2$  in constant false alarm rate (CFAR) detector to the subtracted image with the given ROI. It can provide a signal-to-clutter ratio (SCR) as well as the ROI of the target.

If there is no detection, the wavenumber ( $k_1$ ) of the first spike is decreased by  $\Delta$ , and that of the second spike is increased by  $\Delta$ , the value of which is 13  $cm^{-1}$  in this paper. If there is a detection, each neighboring band image is probed additionally to obtain a maximum signal score.

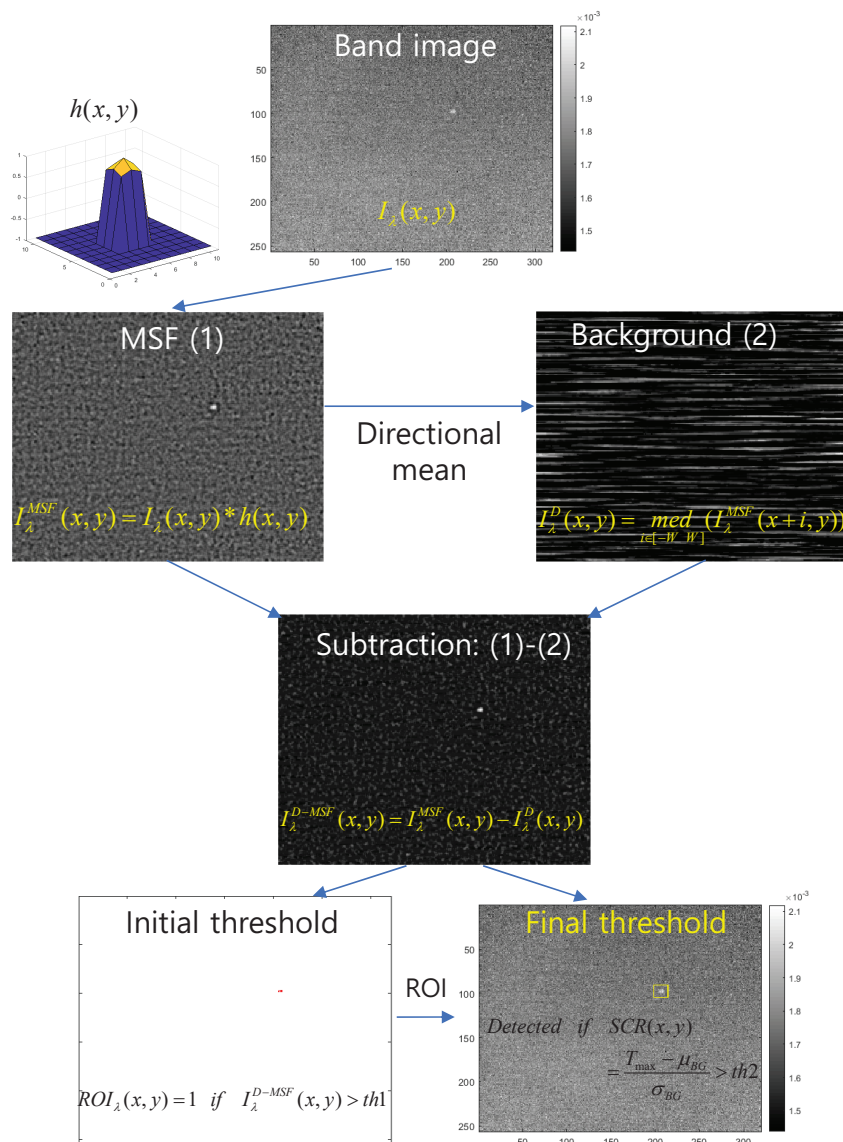


**Figure 6.** Operational flow of the directional-mean subtraction filter (D-MSF) for small-target detection in a band image.

Finally, in Step 3, the joint detection process is performed from the first and second spike detections:  $[x_1, y_1, w_1, h_1, SCR_1], [x_2, y_2, w_2, h_2, SCR_2]$ , where  $[\cdot]$  denotes  $[\text{column, row, width, height, SCR}]$  of the detected target. If two detections exist, then the final target information is merged with Equation (6). If the merged SCR is larger than a predefined threshold ( $th3$ ), then it is declared a final target.

$$Final\ target\ info = \left[ \frac{x_1 + x_2}{2}, \frac{y_1 + y_2}{2}, \frac{w_1 + w_2}{2}, \frac{h_1 + h_2}{2}, (SCR_1 + SCR_2) \right] \quad (6)$$

Figure 7 shows the spectral profile of a remote ship’s plume and an enlarged view focusing on the atmospheric CO<sub>2</sub> absorption band. The numbers (1), (2), (3), and (4) represent the probing band locations of the proposed CO<sub>2</sub>-DS method; (1) and (2) belong to the first spike band, and (3) and (4) belong to the second spike band. Note that the first spike is not clear in remote cases but it does not matter in our CO<sub>2</sub>-DS method since D-MSF is used. Figure 8 shows the corresponding band images, and the max SCR is used to select a band image for each spike: (2) and (3) are selected. The bottom image in Figure 8 represents the result of joint detection from the detection results of the first spike and the second spike.

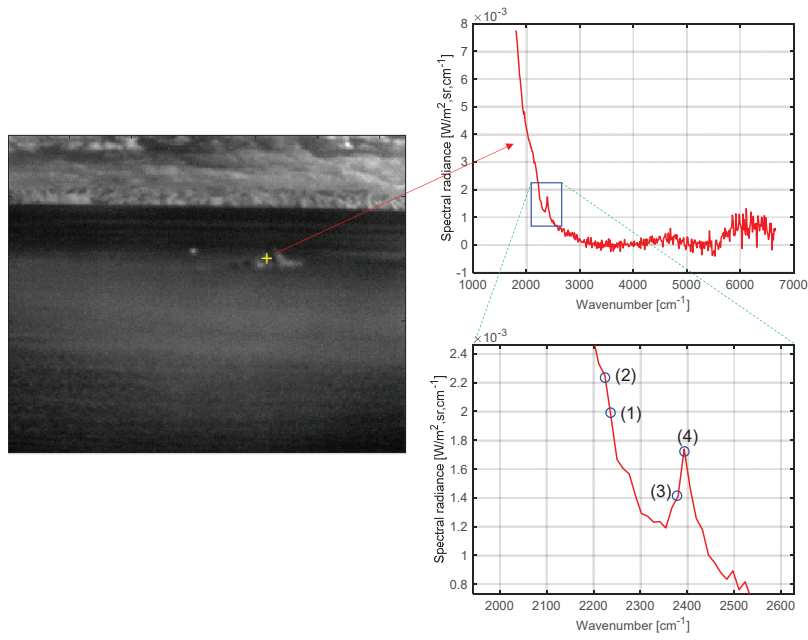


**Figure 7.** Spectral profile of a remote ship’s plume with the probed band positions: first spike: (1) and (2); second spike: (3) and(4).

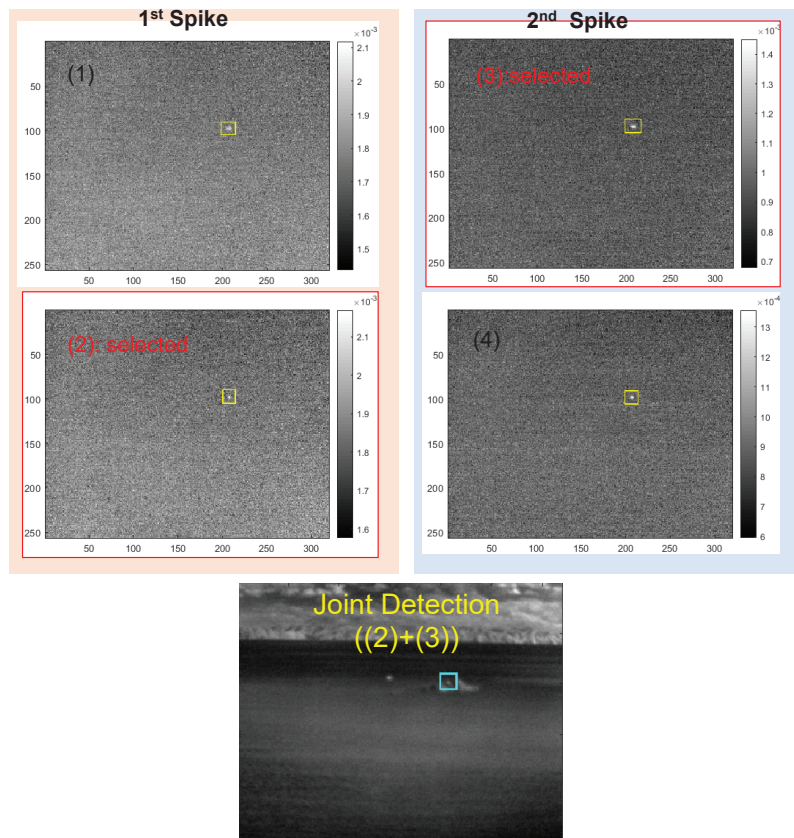


**Figure 8.** Probed band images of first and second spikes corresponding to (1) and (2), and (3) and (4), respectively. The final target is detected via joint detection from the selected max signature for each spike.

### 3. Experimental Results

#### 3.1. Experiment 1: Analysis of Signature Variation

MWIR hyperspectral images of remote ships were acquired with the open path TELOPS Hyper-Cam Mid-Wave Extended (MWE) model [40]. It could provide calibrated spectral radiance images with a high spatial and spectral resolution from a Michelson interferometer in the shortwave to midwave band (1.5–5.6  $\mu\text{m}$ ). The spatial image resolution was  $320 \times 256$ , and the spectral resolution was up to  $0.25 \text{ cm}^{-1}$ . The noise-equivalent spectral radiance (NESR) was  $7 \text{ [nW}/(\text{cm}^2 \cdot \text{sr} \cdot \text{cm}^{-1})]$ , and the radiometric accuracy was approximately 2 K. The field of view was  $6.5 \times 5.1$  degrees.

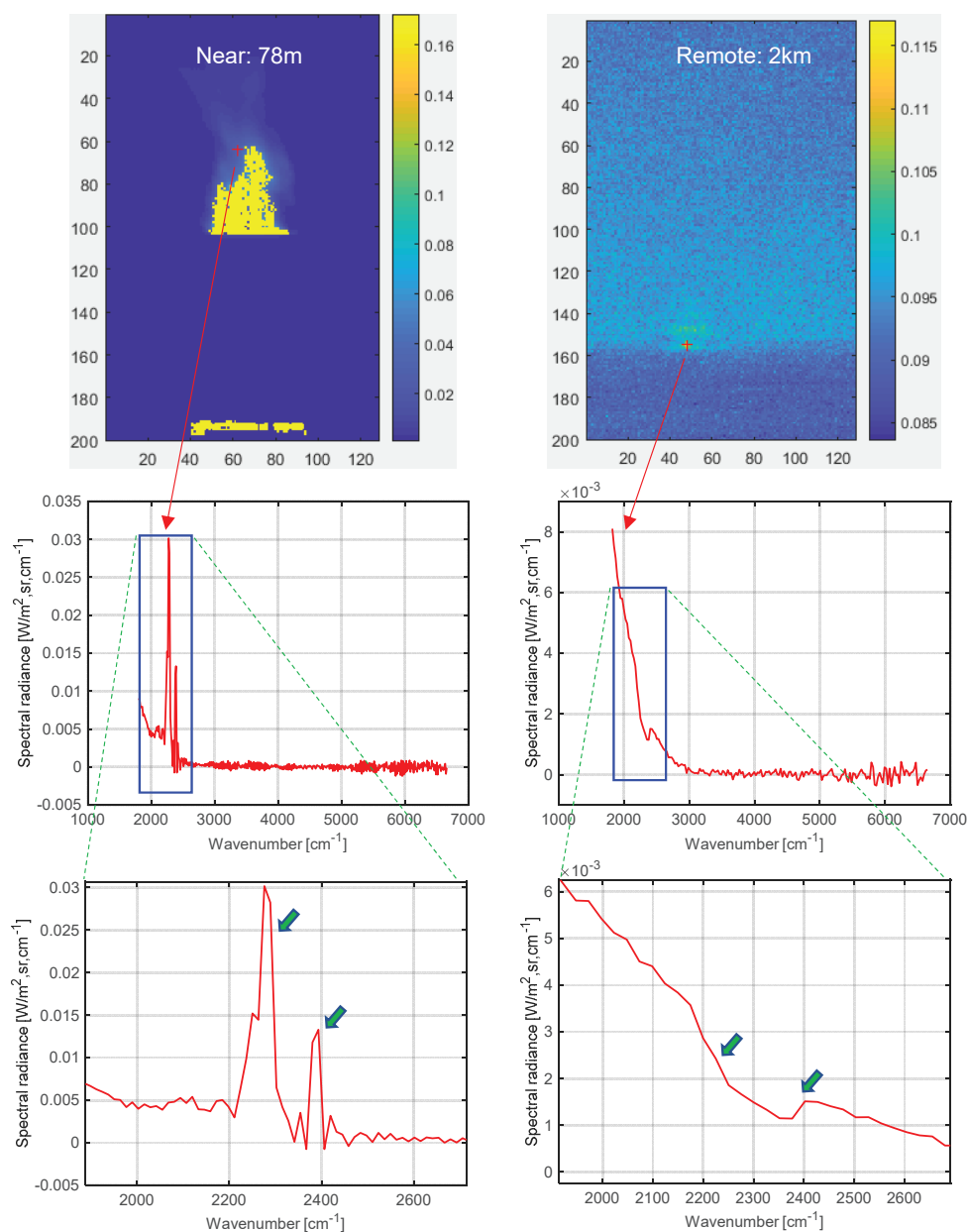


**Figure 9.** Comparison of CO<sub>2</sub> signatures in terms of distance: (left) near CO<sub>2</sub> (78 m), (right) remote CO<sub>2</sub> (2 km).

In the first experiment, the effect of signature variation was compared, depending on target distance. Figure 9 shows the spectral profiles of hot CO<sub>2</sub> plumes, both near (78 m) and remote (2 km).

A strong double-spike phenomenon can be observed for near CO<sub>2</sub>, as shown in Figure 9 (left side) due to relatively weak signal attenuation. However, a remote target does not show such a distinctive double-spike pattern as seen in Figure 9 (right side), which makes it clear that only the spectral profile-based approach was not effective at detecting targets. This conclusion was confirmed through a real experiment applying the well-known spectral angle mapper-based detector [45] to the spectral profiles. Figure 10 shows the spectral profile-based detection results. The left column is the training region; the middle column is a representative spectral profile after training (just the mean of spectral profiles); and the right column is SAM-based detection results indicated by red dots. For the near target, the hot CO<sub>2</sub> plume region could be detected correctly with a similarity threshold of 0.8, as shown in Figure 10a. On the other hand, the remote target signature was unclear, which led to false positive detections with a similarity threshold of 0.98, as shown in Figure 10b.

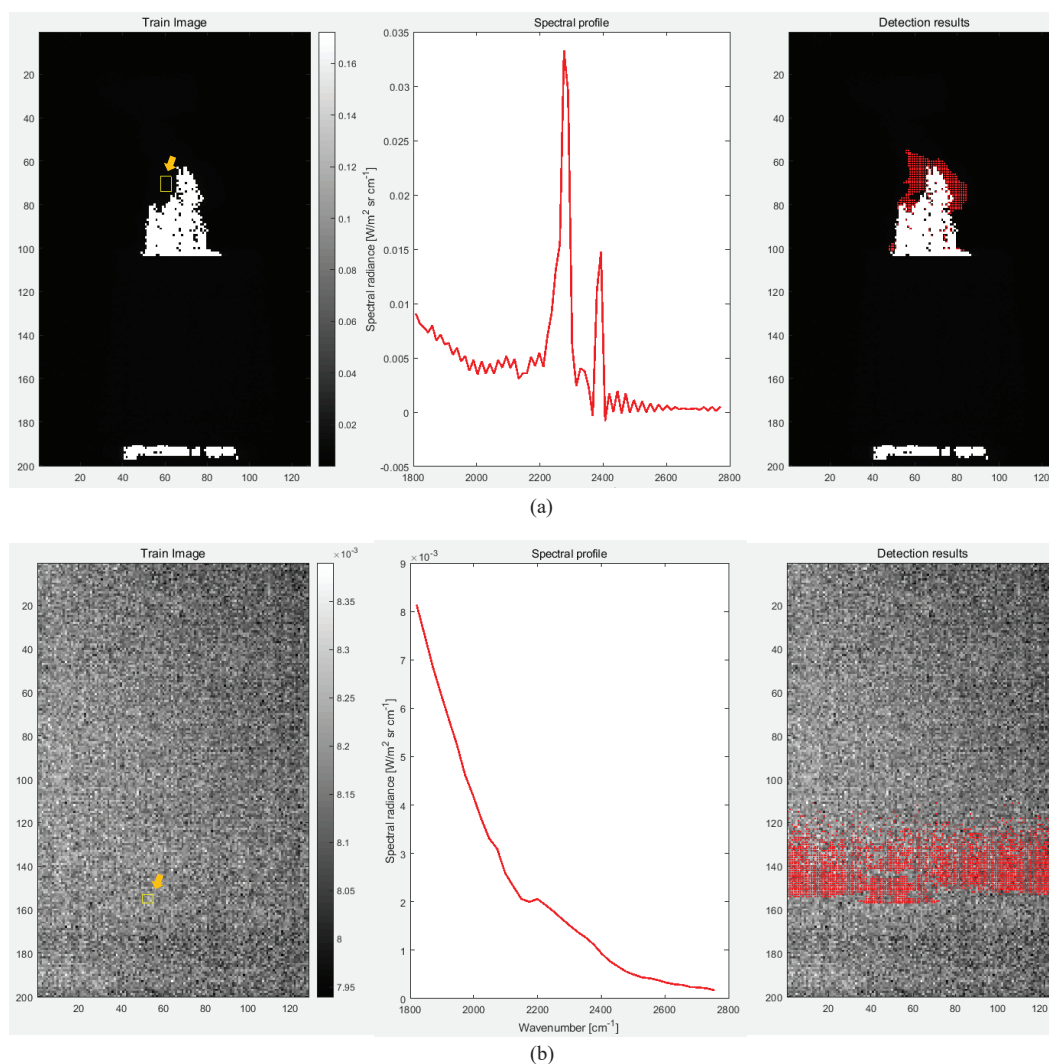


**Figure 10.** Spectral profile-based target detection results: (a) near CO<sub>2</sub>, (b) remote CO<sub>2</sub>.

### 3.2. Experiment 2: Detection Parameter Analysis

In the second experiment, key parameters of the proposed CO<sub>2</sub>-DS method were analyzed and evaluated. There are four parameters; spectral band range for probing, initial threshold (th1) and CFAR threshold (th2) in the D-MSF, and final threshold (th3) from joint detection. The spectral band range for robust ship detection should be determined analytically based on Figure 11. Basically, the atmospheric CO<sub>2</sub> absorption band should be included. Since the air temperature is usually 300 K, this band is

fixed at  $[2320\text{--}2380\text{ cm}^{-1}]$  as shown in the bottom part of Figure 11. The first-spike band starts at  $2300\text{ cm}^{-1}$  and ends at  $2180\text{ cm}^{-1}$  considering band offset. The second-spike band starts at  $2380\text{ cm}^{-1}$  and ends at  $2450\text{ cm}^{-1}$  considering band offset. The band images below  $2180\text{ cm}^{-1}$  or above  $2450\text{ cm}^{-1}$  show background clutter with target information that should be excluded to ensure extremely few false positives.

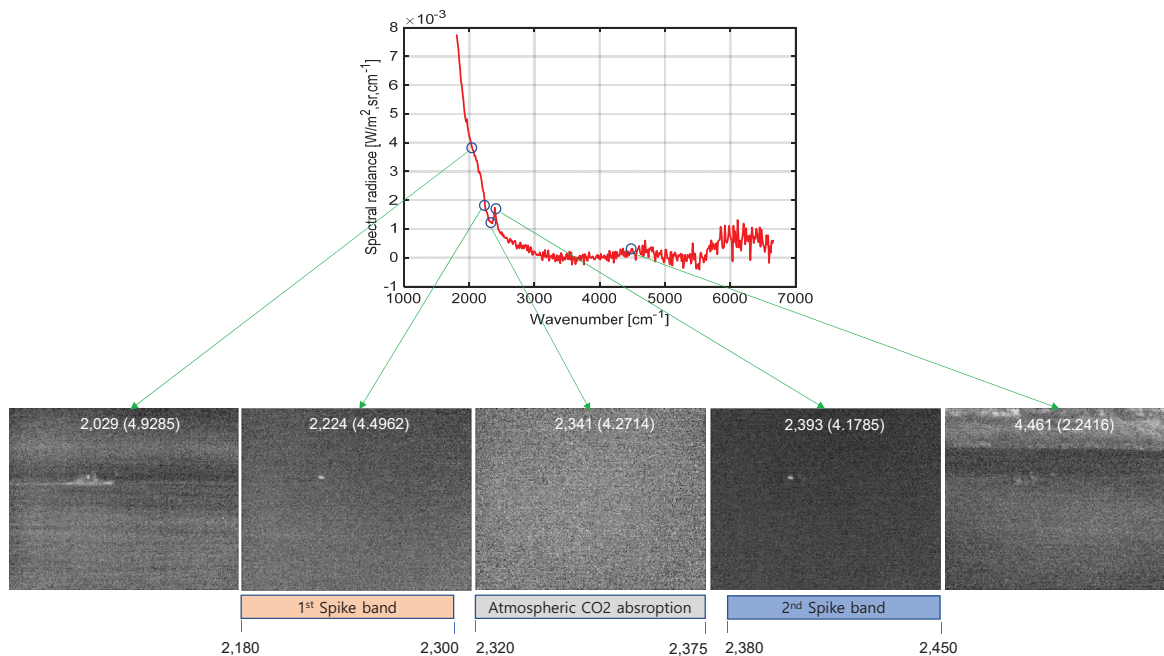


**Figure 11.** Analysis of spectral band ranges for ship detection by visualizing corresponding band images.

The selection of threshold1 ( $th1$ ) is used to determine an ROI in order to investigate whether it is a target or not, as shown in Figure 6. Figure 12 shows the image for  $I_{\lambda}^{MSF}(x, y)$ , where the bright blob represents the hot  $\text{CO}_2$  target, and others are background pixels. The 3D surf views of the target patch and background patch show the signal levels, and the lower left graph of Figure 6 displays the signal intensity profile corresponding to the dotted red line in the image. Note that the max signal is  $20 \times 10^{-5} [\text{W}/\text{m}^2, \text{sr}, \text{cm}^{-1}]$  and the max background signal is  $5 \times 10^{-5} [\text{W}/\text{m}^2, \text{sr}, \text{cm}^{-1}]$ . Considering the safety margin of factor 2,  $th1$  was set at  $1.0 \times 10^{-4} [\text{W}/\text{m}^2, \text{sr}, \text{cm}^{-1}]$ . The threshold 2 parameter ( $th2$ ) can be set by analyzing the SCR values for different targets, as shown in Figure 13. Most SCRs of a spike band image are larger than 12.8, so,  $th2$  can be set at 10.0 for a safe detection capability. The last threshold ( $th3$ ) was varied to calculate the receiver operating characteristic (ROC) curve in order to compare different target-detection methods.

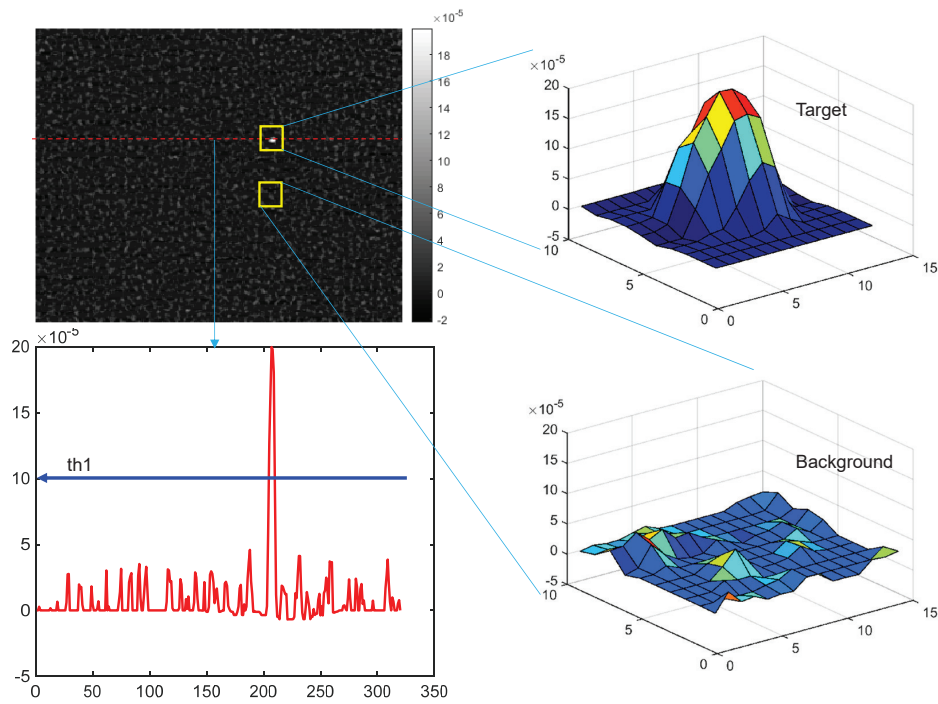


Figure 12. Parameter analysis of threshold 1 ( $th1$ ) from directional mean subtraction image.

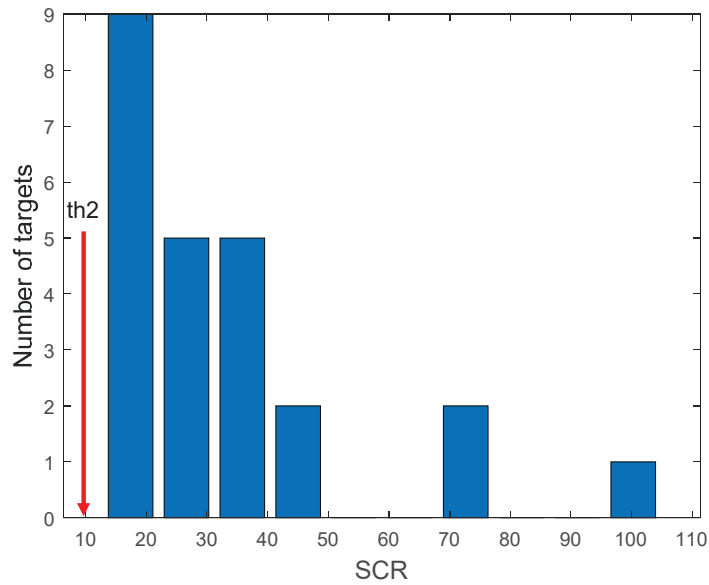


Figure 13. Parameter analysis of threshold 2 ( $th2$ ) from statistics of SCR values of different targets.

### 3.3. Experimental 3: Performance Evaluation

Based on these parameter analyses, the final detection performance was evaluated by comparing the proposed CO<sub>2</sub>-DS, D-MSF [4], and the high-boost multi-scale contrast measure (MLCM) [46]. MLCM is based on the human visual system, and greatly improves the detection rate for small infrared targets. The test images consist of 53 hypercubes acquired by a TELOPS MWIR hyperspectral camera. Three different ships with distance ranges between 1.5 km and 4 km were considered. For the baseline methods, test images were prepared by making broad band images in the spectral range of 3.5–5.6 μm. The ROC metric was used for a fair detection performance based on false positives per image (FPPI). Figure 14 summarizes detection performance. The proposed method (the red solid line) showed

an ideal detection curve. MLCM ranked second, and D-MSF showed the worst result. Visual inspection was conducted at the indicated FPPI (0.65/image). With a normal homogeneous background, the three methods showed reasonable working performance, as seen in Figure 15. Magenta circles represent ground truth, cyan rectangles are detection results from the proposed CO<sub>2</sub>-DS, and yellow rectangles represent baseline detection results. If there was strong cloud clutter, D-MSF generated many false alarms, as shown in Figure 16. In a strong sea-clutter environment, MLCM detected a lot of sea-glints, as shown in Figure 17. Note that the proposed CO<sub>2</sub>-DS showed stable detection results without any false positives from sky or sea clutter. In addition, the ship was located at 4 km (near the horizon) and was detected successfully by our proposed method.

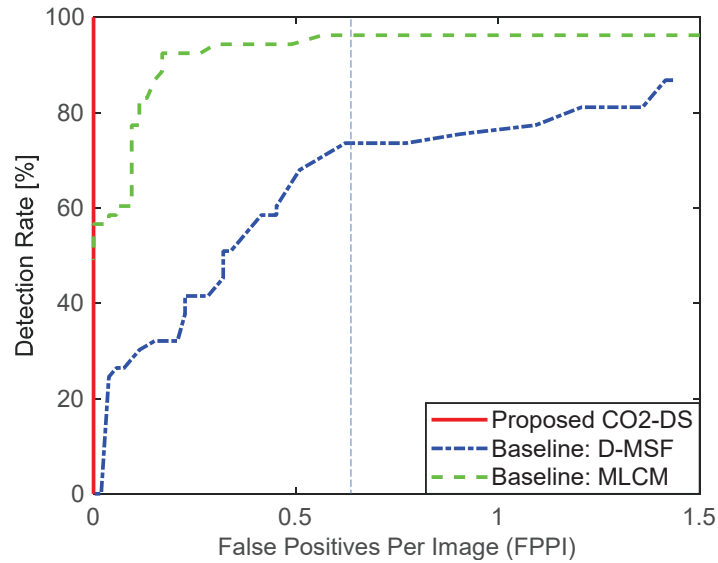


Figure 14. Receiver operating characteristic (ROC)-based comparison of detection performance.

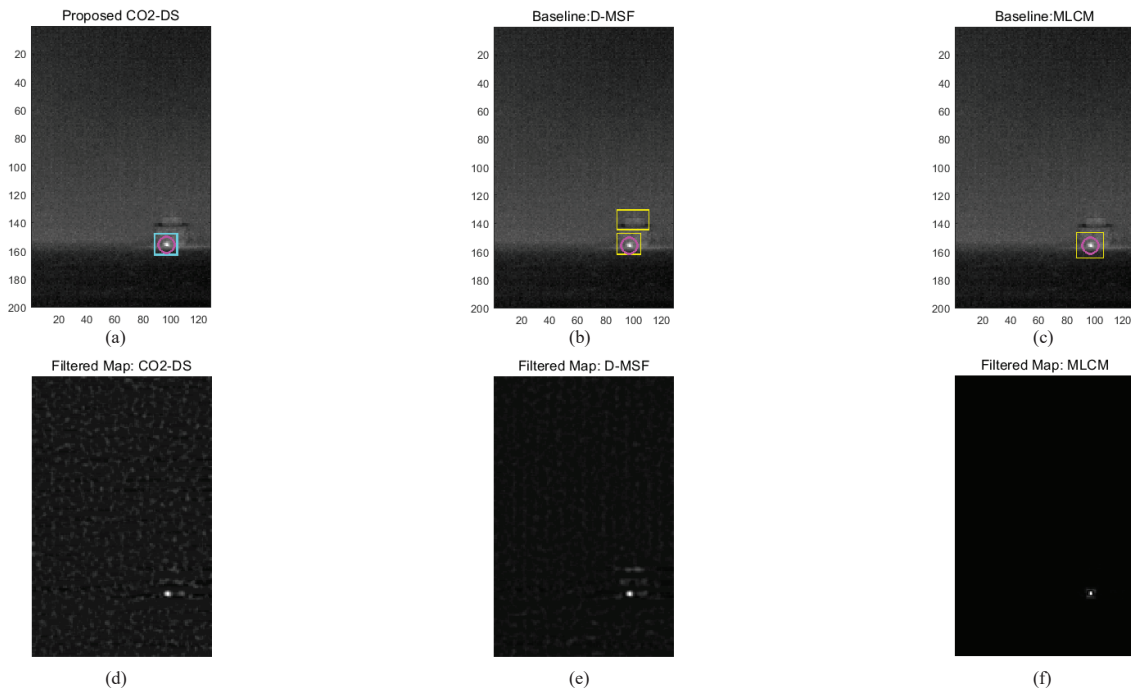
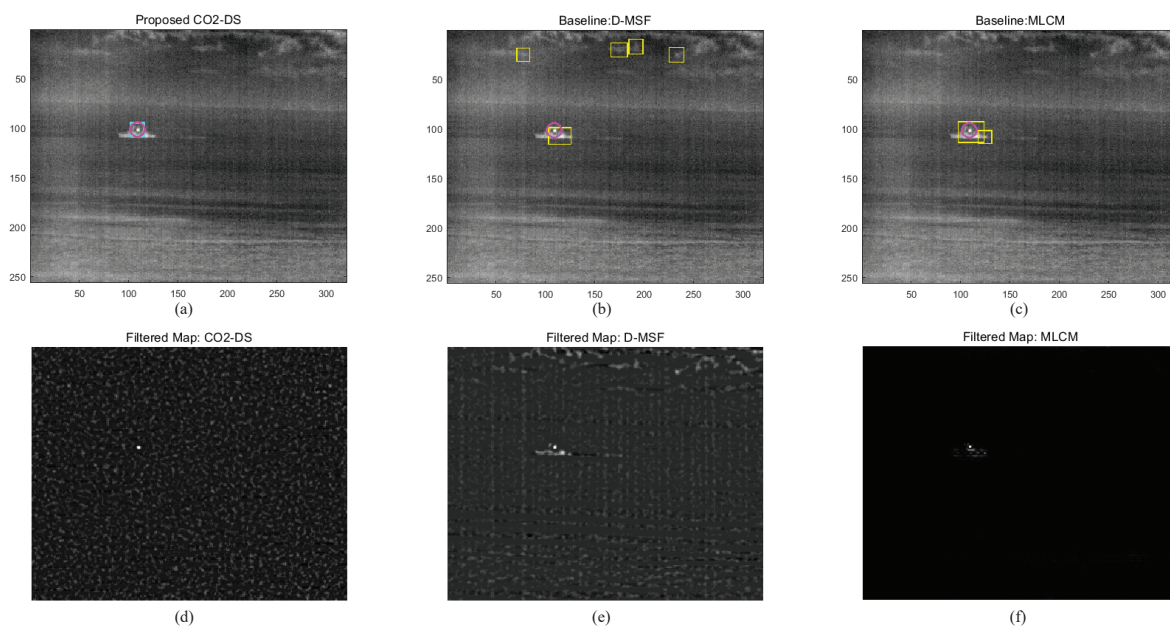
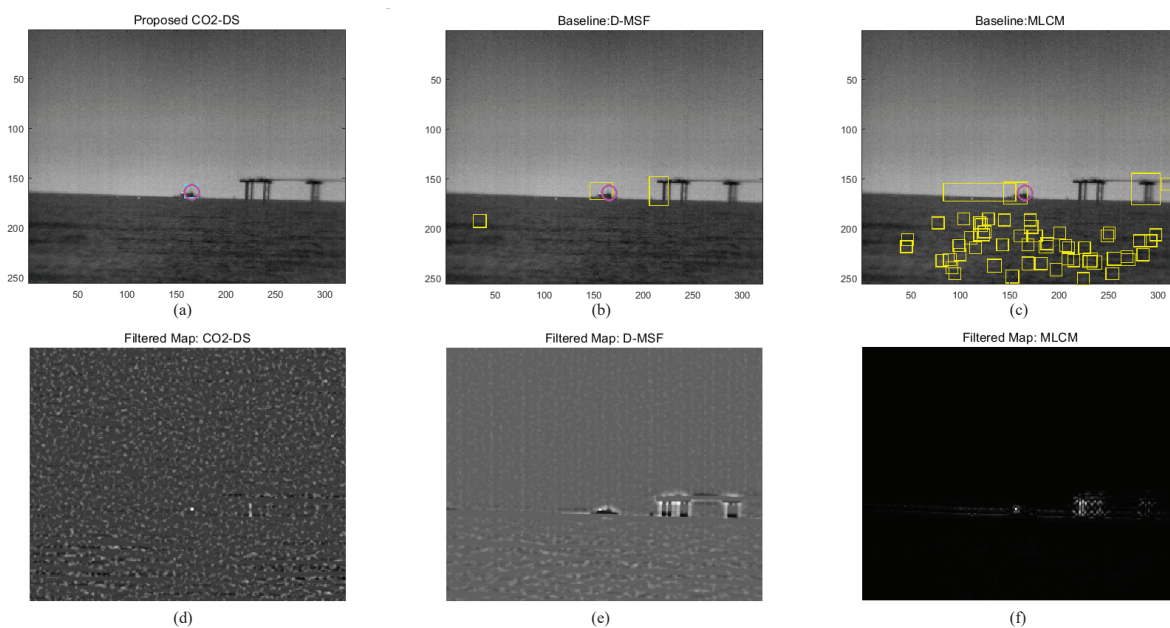


Figure 15. Comparative detection examples for a homogeneous background: (a–c) detection results, (d–f) filtered maps.



**Figure 16.** Comparative detection examples for cloud-clutter backgrounds: (a–c) detection results, (d–f) filtered maps.



**Figure 17.** Comparative detection examples for sea-clutter backgrounds: (a–c) detection results, (d–f) filtered maps.

### 3.4. Experiment 4: Detection Performance Analysis

It can be useful to analyze the effect of weather condition and target distance to the detection performance. The proposed CO<sub>2</sub>-DS method is based on Equation (4), especially atmospheric transmittance ( $\tau(\lambda)$ ). Therefore, if we use the MODTRAN-based atmospheric transmittance calculation and measured background noise, we can conduct the Monte Carlo simulation. Figure 18 represents the MODTRAN-based atmospheric transmittance calculation by changing distance at a specific wavenumber ( $2390.16 \text{ cm}^{-1}$ ) or wavelength ( $4.184 \mu\text{m}$ ). The atmosphere model was selected either

“MidLatitude Summer” or “MidLatitude Winter” to consider the effect of humidity and temperature. The distance length changed from 0.1 km to 6.0 km with 0.1 km interval.

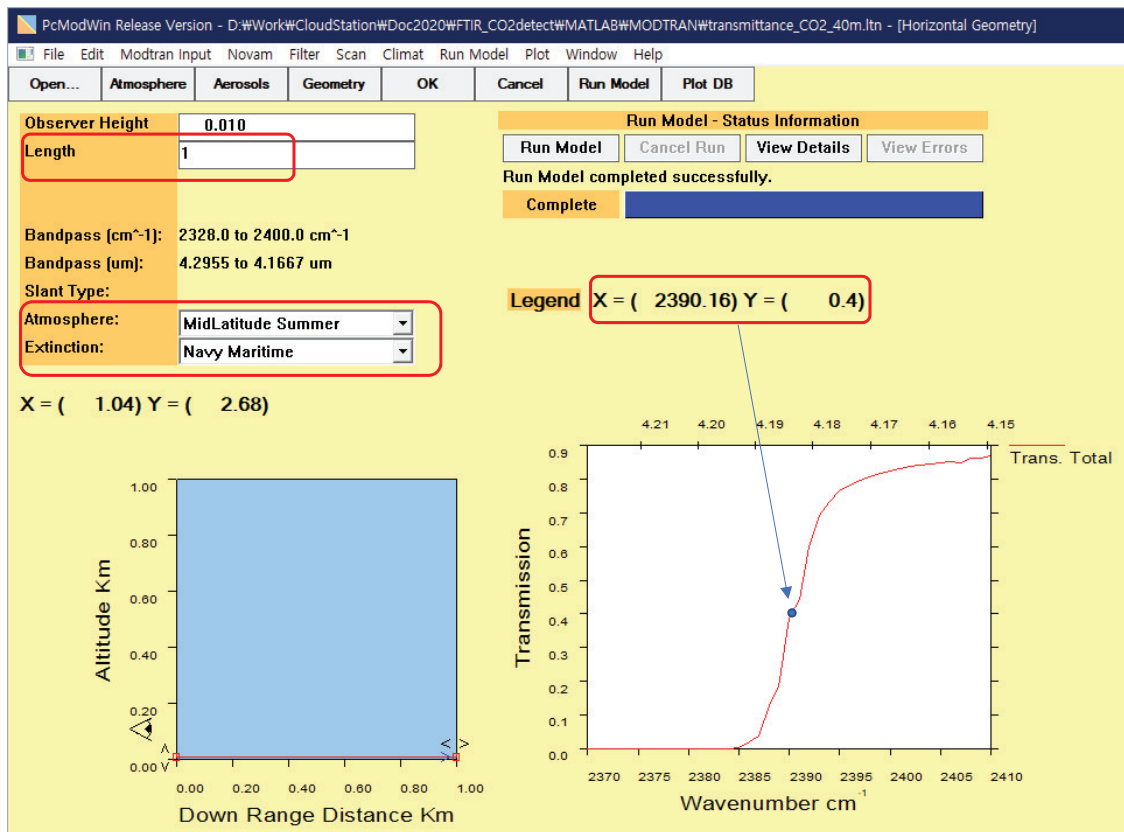


**Figure 18.** Moderate-Resolution Atmospheric Radiance and Transmittance (MODTRAN) environment for atmospheric transmittance calculation.

The proposed CO<sub>2</sub>-MS detector uses target-background difference method (mean subtraction filter). Therefore, the path radiance term can be removed. Figure 19 shows a filtered map for the spectral band image at 2393 cm<sup>-1</sup>. The maximum target signal-background at 2 km is  $6.1742 \times 10^{-4} [\text{W}/\text{m}^2 \cdot \text{sr} \cdot \text{cm}^{-1}]$ . If one uses transmittance of 0.18 at 2 km, the original signal-background is  $3.4 \times 10^{-3} [\text{W}/\text{m}^2 \cdot \text{sr} \cdot \text{cm}^{-1}]$ . Background noise can be modeled as the rectified Gaussian noise model with 0 mean and standard deviation of  $1.3964 \times 10^{-5} [\text{W}/\text{m}^2 \cdot \text{sr} \cdot \text{cm}^{-1}]$ . Th2 (SCR) is set as 10 in this simulation. Figure 20 shows the atmospheric transmittance and Monte Carlo simulation-based detection performance according to the target distance and weather conditions. Normally, the transmittance in mid-latitude summer is lower than that in mid-latitude winter because of higher water vapor contents (higher humidity), which leads to shorten the detection range as Figure 20b. If we fix target distance at 5 km, the detection rate is reduced from 95.4% to 5.2%.

The proposed CO<sub>2</sub>-MS detection method shows extremely low false positives in ship detection. In addition, CO<sub>2</sub>-MS is based on the thresholding and clustering. So, it can detect multiple targets. Because the CO<sub>2</sub>-MS can use both the spectral and spatial information, the size of the ship (fishing boat, military ship, or cargo ship) can be identified if each ship has different type of fuel, engine, gas volume, and temperature. However, it has several limitations such as expensive spectral measurement device, weak to weather condition such as high humidity.

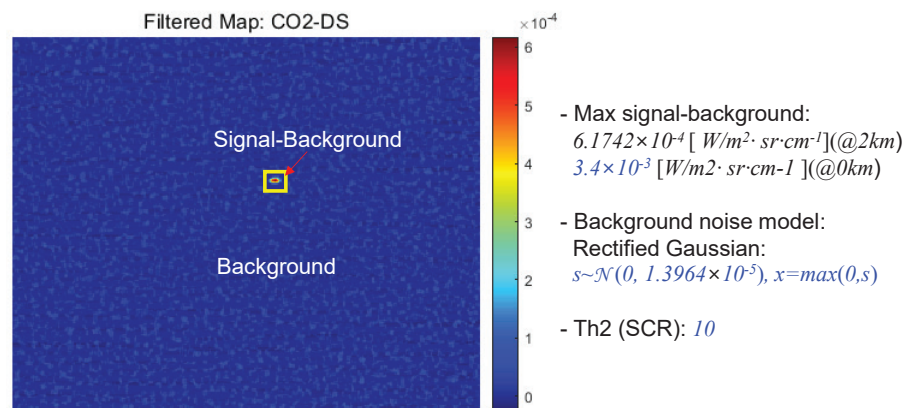


Figure 19. MODTRAN environment for atmospheric transmittance calculation.

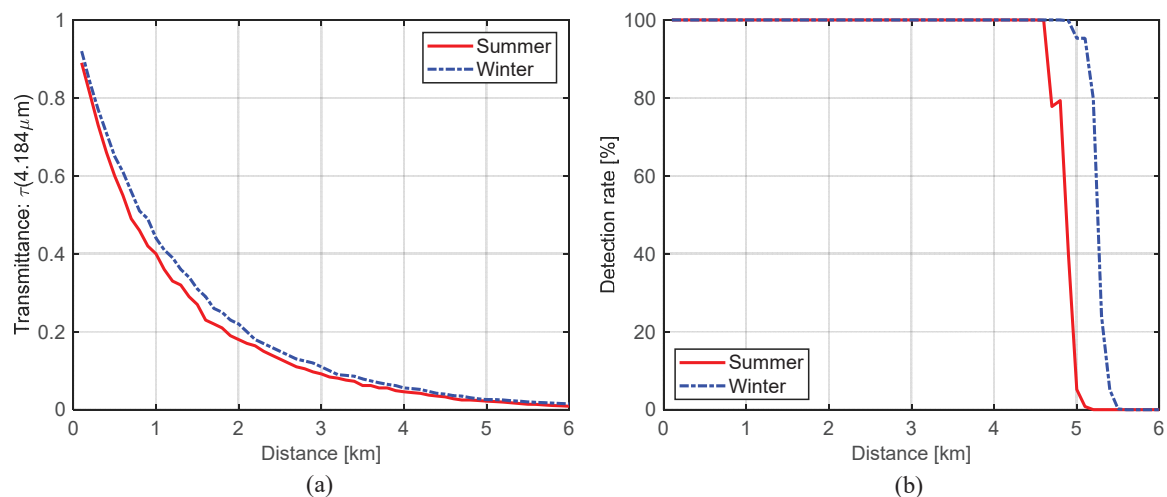


Figure 20. (a) Atmospheric transmittance vs. distance, (b) Monte Carlo simulation-based detection results.

#### 4. Conclusions

Remote-ship detection is important in various applications, such as navigation and surveillance. Midwave infrared image-based ship detection is deployed due to its long-range detection capability in the maritime environment. However, MWIR images show strong response to cloud clutter and sea glint, which generate many false positives, even in state-of-the-art methods. This paper proposed a completely different approach by fusing spectral and spatial information in the MWIR carbon dioxide absorption band with the double-spike phenomenon. The atmospheric CO<sub>2</sub> absorption band (2320–2375 cm<sup>-1</sup>) can block all background radiance, and remote hot CO<sub>2</sub> can penetrate through the spectral double-spike band, which is detected by the proposed carbon dioxide-double spike algorithm. Experimental results in a real cluttered sea environment with remote ships showed excellent detection performance with extremely few false positives if the ships' diesel engines are working.

**Author Contributions:** The contributions were distributed between authors as follows: S.K. (Sungho Kim) wrote the text of the manuscript and programmed the hyperspectral detection method. J.S., J.A. and S.K. (Sunho Kim) provided the midwave infrared hyperspectral database, operational scenario, performed the in-depth discussion of the related literature, and confirmed the accuracy experiments that are exclusive to this paper. All authors have read and agree to the published version of the manuscript.

**Funding:** This research was funded by ADD grant number UE191095FD, 2020 Yeungnam University Research Grants, NRF (NRF-2018R1D1A3B07049069) and the APC was funded by NRF.

**Acknowledgments:** This study was supported by the Agency for Defense Development (UE191095FD). This work was supported by the 2020 Yeungnam University Research Grants. This research was also supported by Basic

Science Research Program through the National Research Foundation of Korea(NRF) funded by the Ministry of Education (NRF-2018R1D1A3B07049069).

**Conflicts of Interest:** The authors declare no conflict of interest.

## References

1. Willburger, K.; Schwenk, K.; Brauchle, J. AMARO—An On-Board Ship Detection and Real-Time Information System. *Sensors* **2020**, *20*, 1324. [[CrossRef](#)] [[PubMed](#)]
2. Brauchle, J.; Bayer, S.; Berger, R. Automatic Ship Detection on Multispectral and Thermal Infrared Aerial Images Using MACS-Mar Remote Sensing Platform. In *Image and Video Technology*; Satoh, S., Ed.; Springer International Publishing: Cham, Switzerland, 2018; pp. 382–395.
3. Li, Y.; Li, Z.; Zhu, Y.; Li, B.; Xiong, W.; Huang, Y. Thermal Infrared Small Ship Detection in Sea Clutter Based on Morphological Reconstruction and Multi-Feature Analysis. *Appl. Sci.* **2019**, *9*, 3786. [[CrossRef](#)]
4. Kim, S.; Lee, J. Small Infrared Target Detection by Region-Adaptive Clutter Rejection for Sea-Based Infrared Search and Track. *Sensors* **2014**, *14*, 13210–13242. [[CrossRef](#)]
5. Xu, F.; Liu, J.; Sun, M.; Zeng, D.; Wang, X. A Hierarchical Maritime Target Detection Method for Optical Remote Sensing Imagery. *Remote Sens.* **2017**, *9*, 280. [[CrossRef](#)]
6. Warren, R.C. Detection of Distant Airborne Targets in Cluttered Backgrounds in Infrared Image Sequences. Ph.D. Thesis, University of South Australia, Sydney, Australia, 2002.
7. Soni, T.; Zeidler, J.R.; Ku, W.H. Performance Evaluation of 2-D Adaptive Prediction Filters for Detection of Small Objects in Image Data. *IEEE Trans. Image Process.* **1993**, *2*, 327–340. [[CrossRef](#)]
8. Sang, H.; Shen, X.; Chen, C. Architecture of a configurable 2-D adaptive filter used for small object detection and digital image processing. *Optical Eng.* **2003**, *48*, 2182–2189. [[CrossRef](#)]
9. Sang, N.; Zhang, T.; Shi, W. Detection of Sea Surface Small Targets in Infrared Images based on Multi-level Filters. *Proc. SPIE* **1998**, *3373*, 123–129.
10. Wang, Y.L.; Dai, J.M.; Sun, X.G.; Wang, Q. An efficient method of small targets detection in low SNR. *J. Phys. Conf. Ser.* **2006**, *48*, 427–430. [[CrossRef](#)]
11. Despande, S.D.; Er, M.H.; Venkateswarlu, R.; Chan, P. Max-Mean and Max-Median Filters for Detection of Small-targets. *Proc. SPIE* **1999**, *3809*, 74–83.
12. Van den Broek, S.P.; Bakker, E.J.; de Lange, D.J.; Theil, A. Detection and Classification of Infrared Decoys and Small Targets in a Sea Background. *Proc. SPIE* **2000**, *4029*, 70–80.
13. Kim, S. Min-local-LoG filter for detecting small targets in cluttered background. *Electron. Lett* **2011**, *47*, 105–106. [[CrossRef](#)]
14. De Lange, H.B.D.J.J.; van den Broek, S.P.; Kemp, R.A.W.; Schwering, P.B.W. Automatic Detection of Small Surface Targets with Electro-Optical Sensors in a Harbor Environment. *Proc. SPIE* **2008**, *7114*, 9–16.
15. Crosby, F. Signature Adaptive Target Detection and Threshold Selection for Constant False Alarm Rate. *J. Electron. Imaging* **2005**, *14*, 1–10. [[CrossRef](#)]
16. Hubbard, W.A.; Page, G.A.; Carroll, B.D.; Manson, D.C. Feature Measurement Augmentation for a Dynamic Programming based IR Target Detection Algorithm in the Naval Environment. *Proc. SPIE* **1999**, *2698*, 2–9.
17. Shirvaikar, M.V.; Trivedi, M.M. A Neural Network Filter to Detect Small Targets in High Clutter Backgrounds. *IEEE Trans. Neural Netw.* **1995**, *6*, 252–257. [[CrossRef](#)] [[PubMed](#)]
18. Lim, E.T.; Shue, L.; Ronda, V. Multi-mode Fusion Algorithm for Robust Dim Point-like Target Detection. *Proc. SPIE* **2003**, *5082*, 94–102.
19. Kojima, A.; Sakurai, N.; Kishigami, J.I. Motion detection using 3D-FFT spectrum. In Proceedings of the IEEE International Conference on Acoustics, Speech, and Signal Processing (ICASSP), Minneapolis, MN, USA, 27–30 April 1993; Volume 5, pp. 213–216.
20. Ye, Z.; Wang, J.; Yu, R.; Jiang, Y.; Zou, Y. Infrared clutter rejection in detection of point targets. *Proc. SPIE* **2002**, *4077*, 533–537.
21. Zuo, Z.; Zhang, T. Detection of Sea Surface Small Targets in Infrared Images based on Multi-level Filters. *Proc. SPIE* **1999**, *3544*, 372–377.
22. Yang, L.; Yang, J.; Yang, K. Adaptive Detection for Infrared Small Target under Sea-sky Complex Background. *Electron. Lett.* **2004**, *40*, 1083–1085. [[CrossRef](#)]

23. Chen, Z.; Wang, G.; Liu, J.; Liu, C. Small Target Detection Algorithm based on Average Absolute Difference Maximum and Background Forecast. *Int. J. Infrared Milli. Waves* **2007**, *28*, 87–97. [[CrossRef](#)]
24. Chi, J.N.; Fu, P.; Wang, D.S.; Xu, X.H. A Detection Method of Infrared Image Small Target based on Order Morphology Transformation and Image Entropy Difference. In Proceedings of the 2005 International Conference on Machine Learning and Cybernetics, Guangzhou, China, 18–21 August 2005; Volume 8, pp. 5111–5116.
25. Rozovskii, B.; Petrov, A. Optimal Nonlinear Filtering for Track-before-Detect in IR Image Sequences. *Proc. SPIE* **1999**, *3809*, 152–163.
26. Silverman, J.; Mooney, J.M.; Cafer, C.E. Tracking Point Targets in Cloud Clutter. *Proc. SPIE* **1997**, *3061*, 496–507.
27. Tzannes, A.P.; Brooks, D.H. Point Target Detection in IR Image Sequences: A Hypothesis-Testing Approach based on Target and Clutter Temporal Profile Modeling. *Opt. Eng.* **2000**, *39*, 2270–2278.
28. Thiam, E.; Shue, L.; Venkateswarlu, R. Adaptive Mean and Variance Filter for Detection of Dim Point-Like Targets. *Proc. SPIE* **2002**, *4728*, 492–502.
29. Kim, S.; Sun, S.G.; Kim, K.T. Highly efficient supersonic small infrared target detection using temporal contrast filter. *Electron. Lett* **2014**, *50*, 81–83. [[CrossRef](#)]
30. Zhang, B.Z.T.; Cao, Z.; Zhang, K. Fast New Small-target Detection Algorithm based on a Modified Partial Differential Equation in Infrared Clutter. *Opt. Eng.* **2007**, *46*, 106401 [[CrossRef](#)]
31. Wu, B.; Ji, H.B. Improved power-law-detector-based moving small dim target detection in infrared images. *Opt. Eng.* **2008**, *47*, 010503. [[CrossRef](#)]
32. Soni, T.; Zeidler, R.; Ku, W.H. Recursive estimation techniques for detection of small objects in infrared image data. In Proceedings of the 1992 IEEE International Conference on Acoustics, Speech, and Signal Processing, San Francisco, CA, USA, 23–26 March 1992; Volume 3, pp. 581–584.
33. Tartakovsky, A.; Blazek, R. Effective adaptive spatial-temporal technique for clutter rejection in IRST. *Proc. SPIE* **2000**, *4048*, 85–95.
34. Lopez-Alonso, J.M.; Alda, J. Characterization of Dynamic Sea Scenarios with Infrared Imagers. *Infrared Phy. Technol.* **2005**, *46*, 355–363. [[CrossRef](#)]
35. Lin, Z.; Ji, K.; Leng, X.; Kuang, G. Squeeze and Excitation Rank Faster R-CNN for Ship Detection in SAR Images. *IEEE Geosci. Remote Sens. Lett.* **2019**, *16*, 751–755. [[CrossRef](#)]
36. An, Q.; Pan, Z.; Liu, L.; You, H. DRBox-v2: An Improved Detector with Rotatable Boxes for Target Detection in SAR Images. *IEEE Trans. Geosci. Remote Sens.* **2019**, *57*, 8333–8349. [[CrossRef](#)]
37. Kang, M.; Ji, K.L.X.L.Z. Contextual Region-Based Convolutional Neural Network with Multilayer Fusion for SAR Ship Detection. *Remote Sens.* **2017**, *9*, 860. [[CrossRef](#)]
38. Yuan, H.; rui Wang, X.; Yuan, Y.; Li, K.; Zhang, C.; shun Zhao, Z. Space-based full chain multi-spectral imaging features accurate prediction and analysis for aircraft plume under sea/cloud background. *Opt. Express* **2019**, *27*, 26027–26043. [[CrossRef](#)]
39. Gagnon, M.; Gagnon, J.; Tremblay, P.; Savary, S.; Farley, V.; Guyot, E.; Lagueux, P.; Chamberland, M. Standoff midwave infrared hyperspectral imaging of ship plumes. In Proceedings of the 2015 7th Workshop on Hyperspectral Image and Signal Processing: Evolution in Remote Sensing (WHISPERS), Tokyo, Japan, 2–5 June 2015; pp. 1–4.
40. Gagnon, M.A.; Gagnon, J.P.; Tremblay, P.; Savary, S.; Farley, V.; Guyot, É.; Lagueux, P.; Chamberland, M. Standoff midwave infrared hyperspectral imaging of ship plumes. *Proc. SPIE* **2016**, *9988*, 998806. [[CrossRef](#)]
41. Romaniello, V.; Spinetti, C.; Silvestri, M.; Buongiorno, M.F. A Sensitivity Study of the 4.8  $\mu\text{m}$  Carbon Dioxide Absorption Band in the MWIR Spectral Range. *Remote Sens.* **2020**, *12*, 172. [[CrossRef](#)]
42. Griffin, M.K.; Hua, K. Burke, H.; Kerekes, J.P. Understanding radiative transfer in the midwave infrared: A precursor to full-spectrum atmospheric compensation. *Proc. SPIE* **2004**, *5425*, 348–356. [[CrossRef](#)]
43. Gagnon, M.A.; Gagnon, J.P.; Tremblay, P.; Savary, S.; Farley, V.; Guyot, E.; Lagueux, P.; Chamberland, M. Standoff midwave infrared hyperspectral imaging of ship plumes. In *Electro-Optical Remote Sensing X*; Kamerman, G., Steinvall, O., Eds.; International Society for Optics and Photonics, SPIE: Bellingham, WA, USA, 2016; Volume 9988, pp. 40–48. [[CrossRef](#)]

44. Schoemaker, R.; Schleijsen, R. Evaluation tools for the effectiveness of infrared countermeasures and signature reduction for ships. In *Infrared Imaging Systems: Design, Analysis, Modeling, and Testing XXI*; Holst, G.C., Krapels, K.A., Eds.; International Society for Optics and Photonics, SPIE: Bellingham, WA, USA, 2010; Volume 7662, pp. 248–257. [[CrossRef](#)]
45. Ibraheem, I. Comparative study of maximum likelihood and spectral angle mapper algorithms used for automated detection of melanoma. *Skin Res. Technol.* **2014**, *21*. [[CrossRef](#)]
46. Shi, Y.; Wei, Y.; Yao, H.; Pan, D.; Xiao, G. High-Boost-Based Multiscale Local Contrast Measure for Infrared Small Target Detection. *IEEE Geosci. Remote Sens. Lett.* **2018**, *15*, 33–37. [[CrossRef](#)]



© 2020 by the authors. Licensee MDPI, Basel, Switzerland. This article is an open access article distributed under the terms and conditions of the Creative Commons Attribution (CC BY) license (<http://creativecommons.org/licenses/by/4.0/>).